# WHAT MATTERS WHEN REPURPOSING DIFFUSION MODELS FOR GENERAL DENSE PERCEPTION TASKS?

**Anonymous authors**
Paper under double-blind review

## ABSTRACT

Extensive pre-training with large data is indispensable for downstream geometry and semantic visual perception tasks. Thanks to large-scale text-to-image (T2I) pretraining, recent works show promising results by simply fine-tuning T2I diffusion models for dense perception tasks. However, several crucial design decisions in this process still lack comprehensive justification, encompassing the necessity of the multi-step stochastic diffusion mechanism, training strategy, inference ensemble strategy, and fine-tuning data quality. In this work, we conduct a thorough investigation into critical factors that affect transfer efficiency and performance when using diffusion priors. Our key findings are: 1) High-quality fine-tuning data is paramount for both semantic and geometry perception tasks. 2) The stochastic nature of diffusion models has a slightly negative impact on deterministic visual perception tasks. 3) Apart from fine-tuning the diffusion model with only latent space supervision, task-specific image-level supervision is beneficial to enhance fine-grained details. These observations culminate in the development of GenPercept, an effective deterministic one-step fine-tuning paradigm tailored for dense visual perception tasks. Different from the previous multi-step methods, our paradigm has a much faster inference speed, and can be seamlessly integrated with customized perception decoders and loss functions for image-level supervision, which is critical to improving the fine-grained details of predictions. Comprehensive experiments on diverse dense visual perceptual tasks, including monocular depth estimation, surface normal estimation, image segmentation, and matting, are performed to demonstrate the remarkable adaptability and effectiveness of our proposed method.

## 1 INTRODUCTION

Recent studies have explored the transferability of text-to-image (T2I) diffusion models to dense visual perception tasks, such as geometry estimation (Ke et al., 2024; Lee et al., 2024; Fu et al., 2024b; Gui et al., 2024; Ye et al., 2024), image segmentation (Van Gansbeke & De Brabandere, 2024; Lee et al., 2024), and inverse rendering (Chen et al., 2024; Kocsis et al., 2024; Zeng et al., 2024). While these works have demonstrated impressive results by repurposing diffusion models for estimating fine-grained geometric and semantic dense prediction maps, the critical design choices made in transferring diffusion models to other dense perception tasks still lack comprehensive justification. This makes it challenging to determine the optimal strategy for achieving the best performance.

For example, Ke et al. (2024) align the visual perception process with the denoising process of Stable Diffusion by fine-tuning all U-Net parameters. They highlight the significance of "multi-resolution noise" in the forward diffusion process during training, aiming to obtain clean predictions by gradually removing Gaussian noise. On the other hand, (Lee et al., 2024) modify the forward diffusion process by interpolating perception annotations with RGB images instead of using Gaussian noise, and only train the low-rank adaptation (LoRA) (Hu et al., 2022) parameters while keeping the U-Net frozen. To the best of our knowledge, the effective components of these approaches have not been thoroughly investigated, leading to uncertainty about which aspects are most crucial for success.

In this work, we examine the design space of repurposing diffusion models for dense visual perception tasks, and explore the key question: **What factors are important when adapting diffusion models for general dense perception tasks?**

To answer this question, we rethink the importance of both fine-tuning protocols and fine-tuning data. From the perspective of fine-tuning protocols, we categorize recent methods into two main groups: *stochastic multi-step generation* and *deterministic multi-step generation*. We explore several critical design spaces, including the diffusion mechanism, key architectural components, training methodologies, and data quality. Our key observations are as follows: **1)** The stochastic nature of diffusion models somewhat conflicts with the deterministic requirements of perception tasks, and the amount of noise used significantly impacts perception performance. **2)** Strict adherence to traditional diffusion processes is unnecessary. Single-step inference provides similar performance with significantly faster execution. **3)** High-quality synthetic fine-tuning data is crucial for geometry perception tasks. From the perspective of fine-tuning data quality, we conduct comprehensive dataset ablation studies on both synthetic datasets and real-world datasets.

Based on the aforementioned observations, we propose GenPercept (see fig. 1), a deterministic fine-tuning paradigm featuring a remarkably simple one-step inference pipeline, an optional customized decoder, and an easily adaptable pixel-specific customized loss. We conduct extensive quantitative and qualitative experiments on a wide range of fundamental visual dense perception tasks, including monocular depth estimation, surface normal estimation, image segmentation, and matting to demonstrate the effectiveness and universality of our method.

In conclusion, our contributions can be summarized as follows: **1)** We systematically analyze the design space of current fine-tuning protocols, considering both model architecture and dataset selection, through comprehensive ablation studies. **2)** Based on these insights, we propose GenPercept, a simple paradigm that harnesses the power of the pre-trained UNet from diffusion models for generalizable dense visual perception tasks.

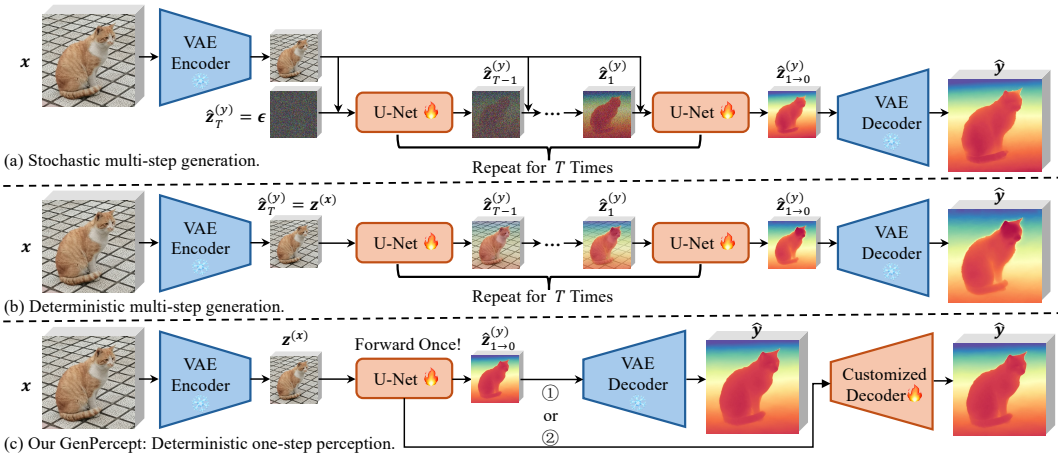


Figure 1: Comparisons of three different pipelines. Our GenPercept enables one-step inference and supports pixel-wise losses and customized decoders to replace the cumbersome VAE decoder. We also extend GenPercept to five dense perception tasks including monocular depth estimation, surface normal estimation, dichotomous image segmentation, semantic segmentation, and image matting.

## 2 PRELIMINARY

Standard diffusion models (Rombach et al., 2022; Chen et al., 2023; Song et al., 2020; Ho et al., 2020) define a forward process to inject Gaussian noise $\boldsymbol{\epsilon}$ into the input data and a reverse denoising process to estimate noises and generate clean images with a denoiser $\boldsymbol{v}_\theta$. While diffusion models generate images from noise, the visual perception tasks take RGB images $\mathbf{x}$ as input and estimate the visual perception labels $\mathbf{y}$. Aiming at transferring the prior knowledge of pre-trained diffusion models to computer vision tasks, previous works have proposed to align with the diffusion process and reformulate visual perception tasks as a multi-step denoising process, especially on the monocular depth estimation task. We review the main high-level ideas of previous algorithms in this section and offer detailed formulations in the supplementary material.

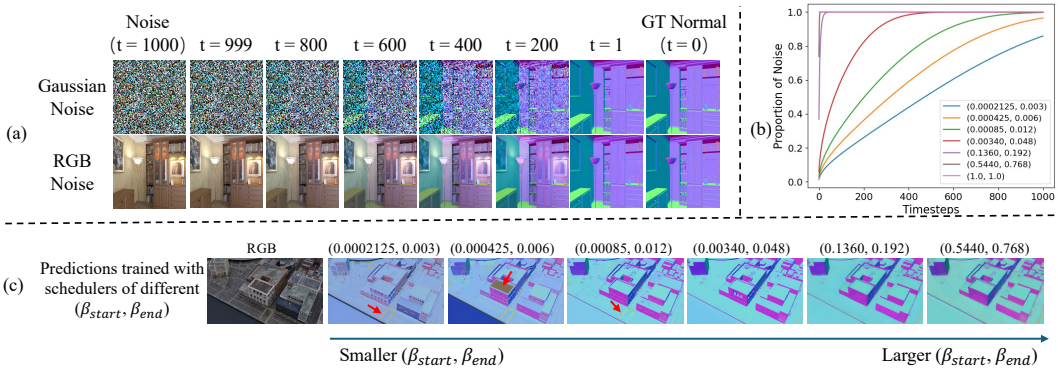


Figure 2: Visualization of different noise forms and proportions in the forward diffusion process. (a) Compared to Gaussian Noise, interpolating RGB images with ground-truth labels can bring less image nature loss. (b) The relationship between the proportion of noise $\sqrt{\bar{\alpha}_t}$ and the ($\beta_{start}$, $\beta_{end}$) hyperparameters. (Please see the supplementary for detailed formulations.) (c) Low $\beta$ values during the training of deterministic multi-step generation will lead to the retention of RGB information. Increasing $\beta$ enhances the training difficulty and addresses this issue.

Recent works mainly explore two alignment choices. For the *stochastic multi-step generation* (Ke et al., 2024; Fu et al., 2024b; Gui et al., 2024), the perception tasks are reframed as an RGB image-conditioned denoising process. For training, they add random Gaussian noise $\boldsymbol{\epsilon}$ to the ground truth latent $\mathbf{z}^{(\mathbf{y})}$ in the forward diffusion process. For inference, the RGB latent $\mathbf{z}^{(\mathbf{x})}$ is concatenated with the noisy depth latent $\hat{\mathbf{z}}_t^{(\mathbf{y})}$ before being sent to U-Net $\boldsymbol{v}_\theta$ for the $t$-th denoising timestep. Clean depth latent $\hat{\mathbf{z}}_0^{(\mathbf{y})}$ will be available after denoising T times. The inference denoising process and forward diffusion process are shown in fig. 1 (a) and fig. 2 (a) separately. These methods perform well but face two significant drawbacks. Firstly, its stochastic nature conflicts with the deterministic nature of perception tasks, which may have a negative impact on performance. Secondly, the high-computation ensemble strategy poses challenges across various perception tasks.

To integrate the deterministic requirements of visual perception tasks with the stochastic diffusion models, *deterministic multi-step generation* methods such as DMP (Lee et al., 2024) reformulate the forward diffusion process as a blending interpolation between RGB images and ground-truth labels. The inference denoising process and training forward diffusion process are shown in fig. 1 (b) and fig. 2 (a), respectively. Although it addresses the uncertainty inherent in the process, the persistence of RGB texture in the generated perception predictions can detrimentally impact accuracy when visualizing the estimated outcomes. This phenomenon is particularly evident in tasks such as surface normal estimation, as exemplified in fig. 2 (c).

## 3 Diffusion Models for Visual Perception Tasks

In this section, we explore the necessity and highlight the findings of the multi-step stochastic diffusion mechanism, prior knowledge hiding behind the architectural components, training strategy, and fine-tuning data quality. The default experimental setting is similar to Ke et al. (2024) and can be found in the supplementary material. We select the stochastic method Marigold (Ke et al., 2024) and the deterministic method DMP (Lee et al., 2024) as our baseline.

### 3.1 The Form and Proportion of Noise in the Forward Diffusion Process

In our initial attempt to integrate the core concepts of Marigold and DMP within a unified codebase, we observed that the "baseline Marigold" performs significantly better than "baseline DMP", and the "multi-resolution noise" strategy introduced by Marigold substantially enhances accuracy. We suppose the noise form and proportion in the forward diffusion process play a critical role.

For the training process, the input of diffusion models is derived from the forward diffusion process, a linear blending process of noise and ground truth with different timesteps and noise forms. To further investigate these phenomena, we illustrate the blending process of representative timesteps in fig. 2(a). For small timesteps like "t = 200", the input blended image still contains part of ground

Table 1: Comprehensive quantitative comparisons about the impact of noise forms and proportions in the forward diffusion process on monocular depth estimation. Visualizations of different noise forms and the effect of $\beta$ values are shown in fig. 2. The performance of DMP improves steadily, while Marigold shows initial improvements followed by a decline. When $\beta$ reaches 1, the inference process can be reduced to one step without compromising performance. "Rank" means the average rank of ten evaluation performance (smaller is better).

| Type | Noise Form | Multi-res Noise | Steps | $(\beta_{start}, \beta_{end})$ | KITTI | | NYU | | ScanNet | | DIODE | | ETH3D | | Rank |
|---|---|---|---|---|---|---|---|---|---|---|---|---|---|---|---|
| | | | | | AbsRel↓ | $\delta_1$↑ | AbsRel↓ | $\delta_1$↑ | AbsRel↓ | $\delta_1$↑ | AbsRel↓ | $\delta_1$↑ | AbsRel↓ | $\delta_1$↑ | |
| Marigold | Gaussian | ✓ | 10 | (0.0002125, 0.003) | 0.358 | 0.462 | 0.297 | 0.555 | 0.246 | 0.625 | 0.494 | 0.565 | 0.267 | 0.640 | 7.0 |
| Marigold | Gaussian | ✓ | 10 | (0.000425, 0.006) | 0.122 | 0.854 | 0.106 | 0.887 | 0.136 | 0.829 | 0.345 | 0.716 | 0.086 | 0.927 | 5.8 |
| baseline Marigold | Gaussian | ✓ | 10 | (0.00085, 0.012) | 0.099 | 0.909 | 0.063 | 0.956 | 0.075 | 0.937 | 0.316 | 0.764 | 0.075 | 0.947 | 3.6 |
| Marigold | Gaussian | ✓ | 10 | (0.0034, 0.048) | 0.100 | 0.906 | 0.057 | 0.963 | 0.063 | 0.957 | 0.308 | 0.768 | 0.074 | 0.948 | 2.3 |
| Marigold | Gaussian | ✓ | 10 | (0.1360, 0.192) | 0.119 | 0.861 | 0.058 | 0.963 | 0.061 | 0.961 | 0.315 | 0.760 | 0.073 | 0.950 | 2.8 |
| Marigold | Gaussian | ✓ | 10 | (0.5440, 0.768) | 0.124 | 0.852 | 0.060 | 0.961 | 0.064 | 0.958 | 0.322 | 0.749 | 0.079 | 0.943 | 4.7 |
| Marigold | Gaussian | ✓ | 10 | (1.0, 1.0) | 0.104 | 0.897 | 0.055 | 0.965 | 0.059 | 0.962 | 0.312 | 0.762 | 0.069 | 0.955 | 1.7 |
| Marigold | Gaussian | ✓ | 1 | (1.0, 1.0) | 0.104 | 0.897 | 0.055 | 0.965 | 0.059 | 0.962 | 0.312 | 0.762 | 0.069 | 0.955 | - |
| Marigold | Gaussian | × | 10 | (0.0002125, 0.003) | 0.587 | 0.255 | 0.337 | 0.490 | 0.257 | 0.604 | 0.600 | 0.469 | 0.372 | 0.503 | 7.0 |
| Marigold | Gaussian | × | 10 | (0.000425, 0.006) | 0.536 | 0.289 | 0.313 | 0.527 | 0.248 | 0.621 | 0.565 | 0.499 | 0.328 | 0.575 | 6.0 |
| baseline Marigold | Gaussian | × | 10 | (0.00085, 0.012) | 0.153 | 0.807 | 0.162 | 0.802 | 0.187 | 0.737 | 0.411 | 0.641 | 0.157 | 0.826 | 5.0 |
| Marigold | Gaussian | × | 10 | (0.0034, 0.048) | 0.101 | 0.907 | 0.058 | 0.963 | 0.066 | 0.954 | 0.309 | 0.765 | 0.074 | 0.950 | 2.4 |
| Marigold | Gaussian | × | 10 | (0.1360, 0.192) | 0.115 | 0.870 | 0.056 | 0.965 | 0.060 | 0.961 | 0.313 | 0.763 | 0.072 | 0.953 | 2.3 |
| Marigold | Gaussian | × | 10 | (0.5440, 0.768) | 0.124 | 0.848 | 0.059 | 0.963 | 0.063 | 0.958 | 0.318 | 0.752 | 0.077 | 0.946 | 3.7 |
| Marigold | Gaussian | × | 10 | (1.0, 1.0) | 0.102 | 0.901 | 0.054 | 0.966 | 0.059 | 0.962 | 0.312 | 0.762 | 0.071 | 0.955 | 1.5 |
| Marigold | Gaussian | × | 1 | (1.0, 1.0) | 0.102 | 0.901 | 0.054 | 0.966 | 0.059 | 0.962 | 0.312 | 0.762 | 0.071 | 0.955 | - |
| DMP | RGB | × | 10 | (0.0002125, 0.003) | 0.476 | 0.336 | 0.267 | 0.601 | 0.216 | 0.677 | 0.457 | 0.588 | 0.185 | 0.757 | 6.9 |
| DMP | RGB | × | 10 | (0.000425, 0.006) | 0.265 | 0.630 | 0.201 | 0.072 | 0.195 | 0.717 | 0.386 | 0.674 | 0.116 | 0.880 | 6.1 |
| baseline DMP | RGB | × | 10 | (0.00085, 0.012) | 0.134 | 0.837 | 0.117 | 0.871 | 0.147 | 0.808 | 0.353 | 0.721 | 0.093 | 0.919 | 5.0 |
| DMP | RGB | × | 10 | (0.0034, 0.048) | 0.107 | 0.890 | 0.077 | 0.939 | 0.087 | 0.923 | 0.318 | 0.766 | 0.078 | 0.940 | 3.8 |
| DMP | RGB | × | 10 | (0.1360, 0.192) | 0.107 | 0.890 | 0.063 | 0.959 | 0.068 | 0.955 | 0.305 | 0.773 | 0.073 | 0.948 | 2.2 |
| DMP | RGB | × | 10 | (0.5440, 0.768) | 0.106 | 0.897 | 0.061 | 0.959 | 0.066 | 0.952 | 0.309 | 0.768 | 0.075 | 0.945 | 2.3 |
| DMP | RGB | × | 10 | (1.0, 1.0) | 0.100 | 0.902 | 0.053 | 0.966 | 0.059 | 0.961 | 0.309 | 0.768 | 0.068 | 0.956 | 1.2 |
| Our baseline | RGB | × | 1 | (1.0, 1.0) | 0.100 | 0.902 | 0.053 | 0.966 | 0.059 | 0.961 | 0.309 | 0.768 | 0.068 | 0.956 | - |

truth information (e.g., the purple color of the surface normal) and may lead to a "ground truth leakage" problem. On the other hand, the blending proportion is controlled by the beta values $(\beta_{start}, \beta_{end})$ of the diffusion model DDPM scheduler. As shown in Figure 2(b) and Figure 2 of the supplementary, increasing the beta values can decrease the ground truth proportion. Training with larger beta values can consistently achieve better performance for both Gaussian noise and RGB noise, which is proved in Table 1 and Figure 2(c). Therefore, we attempt to increase the values of $(\beta_{start}, \beta_{end})$ to reduce the proportion of ground truth in the blending process.

Our quantitative and qualitative analyses, presented in table 1 and fig. 2(c), indicate that "preventing the ground truth leakage" leads to improved model performance. As the $\beta$ value increases, the impact of "multi-resolution noise" diminishes. However, unlike DMP, which continues to show performance improvements, Marigold's performance begins to be slightly unstable but shows a rough improvement trend when the $\beta$ value is sufficiently high. We consider it brought by the randomness of the Gaussian Noise, which dominates most components of the input latent.

When $\beta$ reaches 1, the noisy label latent input effectively becomes a pure noise latent, akin to the RGB latent in DMP. Consequently, the target output of the "v-prediction" diffusion model shifts to the negative value of the ground truth latent, eliminating any intermediate state of blending between RGB noise latent and ground-truth latent. The denoising process becomes repeats of "predict target label $\hat{\mathbf{z}}_0^{(\mathbf{y})}$ from RGB image $\mathbf{z}^{(\mathbf{x})}$ and add (RGB) noise back to the RGB image $\mathbf{z}^{(\mathbf{x})}$", whose estimation results in any timestep $t$ are exactly identical. Therefore, we propose to reduce the DDIM steps to one and call it "deterministic one-step perception". The resulting inference speeds are significantly faster, with performance remaining largely consistent. We consider it as "our baseline" for the subsequent analyses. Please see the formulation of supplementary material for details.

> ***Finding* 1.** The inherent stochasticity of diffusion models can lead to minor, unstable performance fluctuations in deterministic perception tasks. By increasing the noise proportion, the multi-step generation can be simplified to a one-step fine-tuning paradigm without any loss of performance in both stochastic and deterministic methods.

### 3.2 Where Does the Rich Visual Knowledge Reside in Diffusion Models?

Based on the baseline we proposed in §3.1, we conduct detailed ablation studies to thoroughly investigate the necessity of each component of Stable Diffusion. Results are reported in table 2.

**Denoiser.** We reinitialize the U-Net parameter and train it from scratch on the same datasets. Without prior knowledge of large data from LAION-5B, the network performs poorly and loses the generalization. This indicates that most of the prior knowledge is stored in the denoiser module.

Table 2: Explorations on the impact of the Stable Diffusion components on depth estimation. Customized decoders and losses can also enable inference acceleration and performance improvement.

| Setting | Loss | KITTI | | NYU | | ScanNet | | DIODE | | ETH3D | |
|---|---|---|---|---|---|---|---|---|---|---|---|
| | | AbsRel↓ | $\delta_1$↑ | AbsRel↓ | $\delta_1$↑ | AbsRel↓ | $\delta_1$↑ | AbsRel↓ | $\delta_1$↑ | AbsRel↓ | $\delta_1$↑ |
| Our baseline | MSE (Latent) | 0.100 | 0.902 | 0.053 | 0.966 | 0.059 | 0.961 | 0.309 | 0.768 | 0.068 | 0.956 |
| Train U-Net from scratch | MSE (Latent) | 0.219 | 0.650 | 0.186 | 0.736 | 0.183 | 0.729 | 0.426 | 0.614 | 0.185 | 0.741 |
| Train VAE decoder from scratch | MSE (Image) | 0.096 | 0.916 | 0.055 | 0.964 | 0.058 | 0.964 | 0.302 | 0.759 | 0.071 | 0.950 |
| Baseline + Image MSE loss | MSE (Image) | 0.097 | 0.915 | 0.054 | 0.964 | 0.059 | 0.964 | 0.305 | 0.760 | 0.071 | 0.953 |
| Baseline + Image customized loss | MSE + SSI + Grad. (Image) | 0.094 | 0.923 | 0.052 | 0.966 | 0.056 | 0.965 | 0.302 | 0.767 | 0.066 | 0.967 |
| Train DPT decoder from scratch | MSE (Image) | 0.099 | 0.912 | 0.055 | 0.964 | 0.058 | 0.963 | 0.302 | 0.759 | 0.069 | 0.956 |

**VAE AutoEncoder.** The VAE encoder's original architecture is kept intact to maintain the consistency of the encoding process. For the VAE decoder, we train it from scratch with image pixel MSE loss. Without pre-trained parameters of the VAE decoder, it still performs well.

**Customized Head and Loss.** The deterministic one-step perception pipeline enables customized heads and loss functions. By utilizing a DPT decoder (Ranftl et al., 2021) and the loss functions of DepthAnythingv2 (Yang et al., 2024b), we can implement a lightweight decoder that supervises pixel-wise information at a higher resolution rather than latent features at 1/8 resolution. This approach can accelerate inference times and enhance the acquisition of fine-grained details.

> ***Finding* 2.** The primary perceptual prior knowledge of diffusion models is encapsulated within the denoiser. Customized heads and loss functions can achieve enhanced inference speed and fine-grained details.

### 3.3 What About the Timesteps and Text Prompts?

The timesteps and text prompts are crucial elements in utilizing the Stable Diffusion model to generate diverse images. We conducted ablation studies to investigate their significance. The results reported in table 3 indicate a negligible difference between various settings. Owing to the inherent certainty associated with visual perception tasks, the diversity typically offered by the textual inputs appears to be unnecessary. Similarly, the utility of timesteps is reduced, as the single-step paradigm does not require progressive denoising.

Table 3: Quantitative comparisons among different timesteps and text prompts on depth estimation.

| Setting | Text Prompt | Train / Infer Timesteps | KITTI | | NYU | | ScanNet | | DIODE | | ETH3D | |
|---|---|---|---|---|---|---|---|---|---|---|---|---|
| | | | AbsRel↓ | $\delta_1$↑ | AbsRel↓ | $\delta_1$↑ | AbsRel↓ | $\delta_1$↑ | AbsRel↓ | $\delta_1$↑ | AbsRel↓ | $\delta_1$↑ |
| Our baseline | "" | Random / 1 | 0.100 | 0.902 | 0.053 | 0.966 | 0.059 | 0.961 | 0.309 | 0.768 | 0.068 | 0.956 |
| Valid text input | "A high quality RGB image" | Random / 1 | 0.101 | 0.900 | 0.053 | 0.967 | 0.058 | 0.964 | 0.312 | 0.762 | 0.070 | 0.954 |
| Random text input | "F3@qV!k2*#Zp^n%1Lz" | Random / 1 | 0.099 | 0.904 | 0.054 | 0.965 | 0.059 | 0.963 | 0.311 | 0.763 | 0.069 | 0.955 |
| Timestep1 | "" | 1 / 1 | 0.100 | 0.906 | 0.054 | 0.965 | 0.060 | 0.961 | 0.304 | 0.769 | 0.069 | 0.956 |
| Timestep500 | "" | 500 / 500 | 0.102 | 0.897 | 0.053 | 0.966 | 0.059 | 0.961 | 0.307 | 0.765 | 0.068 | 0.956 |
| Timestep900 | "" | 900 / 900 | 0.105 | 0.891 | 0.054 | 0.966 | 0.058 | 0.964 | 0.309 | 0.762 | 0.068 | 0.953 |

> ***Finding* 3.** The timesteps and text prompts of diffusion models are negligible for the performance of visual perception tasks.

### 3.4 How to Leverage the U-Net's Prior Knowledge?

The significance of the denoiser cannot be overstated. However, the strategies for its utilization are worth careful consideration. Should we freeze the denoiser, utilize its intermediate features, and merely fine-tune the decoder for specific tasks? Alternatively, could we employ LoRA (Hu et al., 2022) instead of extensively fine-tuning the entire denoiser? Unfortunately, the evidence suggests that neither approach is ideal. As illustrated in table 4, freezing the denoiser significantly compromises performance. Although incorporating LoRA offers some advantages, it can not fully leverage the potential of denoiser, especially with regular LoRA ranks of 4 and 16. This limitation likely stems from the substantial differences between the noise-to-image denoising process and the image-to-perception prediction task.

> ***Finding* 4.** Fine-tuning the denoiser is preferable compared to either merely utilizing its intermediate features or training it with LoRA.

Table 4: Explorations on the paradigms to leverage U-Net's prior knowledge on depth estimation.

| Setting | LoRA Rank | KITTI | | NYU | | ScanNet | | DIODE | | ETH3D | |
|---|---|---|---|---|---|---|---|---|---|---|---|
| | | AbsRel↓ | $\delta_1$↑ | AbsRel↓ | $\delta_1$↑ | AbsRel↓ | $\delta_1$↑ | AbsRel↓ | $\delta_1$↑ | AbsRel↓ | $\delta_1$↑ |
| Our baseline | - | 0.100 | 0.902 | 0.053 | 0.966 | 0.059 | 0.961 | 0.309 | 0.768 | 0.068 | 0.956 |
| Freeze U-Net + Train DPT decoder | - | 0.144 | 0.803 | 0.086 | 0.931 | 0.097 | 0.911 | 0.309 | 0.768 | 0.068 | 0.956 |
| Train U-Net with LoRA | 4 | 0.211 | 0.644 | 0.095 | 0.914 | 0.100 | 0.902 | 0.372 | 0.689 | 0.121 | 0.864 |
| Train U-Net with LoRA | 16 | 0.166 | 0.746 | 0.085 | 0.931 | 0.087 | 0.927 | 0.352 | 0.712 | 0.104 | 0.901 |
| Train U-Net with LoRA | 64 | 0.138 | 0.817 | 0.077 | 0.944 | 0.079 | 0.940 | 0.336 | 0.734 | 0.089 | 0.930 |
| Train U-Net with LoRA | 256 | 0.133 | 0.827 | 0.069 | 0.952 | 0.073 | 0.947 | 0.325 | 0.745 | 0.088 | 0.933 |
| Train U-Net with LoRA | 1024 | 0.125 | 0.849 | 0.067 | 0.955 | 0.074 | 0.947 | 0.324 | 0.747 | 0.084 | 0.939 |

Table 5: Investigations into the impact of training data quality on depth estimation.

| Data Quality | Datasets | KITTI | | NYU | | ScanNet | | DIODE | | ETH3D | |
|---|---|---|---|---|---|---|---|---|---|---|---|
| | | AbsRel↓ | $\delta_1$↑ | AbsRel↓ | $\delta_1$↑ | AbsRel↓ | $\delta_1$↑ | AbsRel↓ | $\delta_1$↑ | AbsRel↓ | $\delta_1$↑ |
| Synthetic Data | Hypersim (50K) + Virtual KITTI (40K) | 0.100 | 0.902 | 0.053 | 0.966 | 0.059 | 0.961 | 0.309 | 0.768 | 0.068 | 0.956 |
| Real Data | Taskonomy (50K) + Cityscapes (40K) | 0.123 | 0.857 | 0.055 | 0.966 | 0.062 | 0.958 | 0.293 | 0.762 | 0.074 | 0.947 |

### 3.5 Is the Training Data Quality Essential?

The quality of annotations in real datasets is often lower compared to synthetic datasets, where data is precisely rendered via simulators. In table 5, we explore the impact of data quality on the fine-tuning process. We sample the same distribution of real data, consisting of 90% from approximately 50K indoor images from the Taskonomy dataset (Zamir et al., 2018) and 10% from about 40K outdoor images from the Cityscapes dataset (Cordts et al., 2016). With lower annotation quality, the model achieves slightly worse performance. Also, the visualization in the supplementary material indicates that noisy data significantly influences detailed predictions in visual perception tasks.

***Finding* 5.** Data quality affects the fine-grained details of dense predictions significantly.

### 3.6 Summary of the Obervations

Based on the preceding analysis, an effective approach to leveraging the prior knowledge of diffusion models is to use them as single-step deterministic perception estimators. This can be done with either a VAE decoder or a customized lightweight decoder. Additionally, employing pixel-specific customized losses can further enhance detail and overall performance. We compare our deterministic single-step perception method with previous multi-step paradigms in fig. 1. In the following section, we extend these findings to a broader set of visual perception tasks, including surface normal estimation, semantic image segmentation, dichotomous image segmentation, and image matting.

## 4 Experiments on Various Dense Visual Perceptual Tasks

In this section, we empirically show the robust transfer ability of our GenPercept on diverse visual tasks. Unless specified otherwise, we freeze the VAE AutoEncoder and fine-tune the U-Net of Stable Diffusion v2.1 to estimate the ground-truth label latent for 30000 iterations, with a resolution of (768, 768), a batch size of 32, and a learning rate of 3e-5. Different customized loss functions are utilized to improve the performance further on dense visual perception tasks.

### 4.1 Geometric Estimation

For geometry evaluation, the ensemble size, inference resolution, valid evaluation depth range (specific for depth estimation), and evaluation average paradigm (average by pixels or average by the number of images) can be different for each method. To compare these approaches fairly, we follow the open-source evaluation code of Marigold (Ke et al., 2024) for depth and DSINE (Bae & Davison, 2024) for surface normal, and evaluate the performance of existing SOTA methods with their officially released model weights.

**Monocular Depth Estimation.** The monocular depth estimation aims to predict the vertical distance between the observed object and the camera from an RGB image. The estimated depth is formulated as affine-invariant depth (Yin et al., 2021; Ranftl et al., 2020; 2021), and should be recovered by performing least square regression with the ground truth. The evaluation is performed on five zero-shoft datasets including KITTI (Geiger et al., 2013), NYU (Silberman et al., 2012), ScanNet (Dai et al., 2017), DIODE (Vasiljevic et al., 2019), and ETH3D (Schops et al., 2017). We

Table 6: Quantitative comparison of affine-invariant depth estimation on five zero-shot datasets.

| Method | Training Samples | KITTI | | NYU | | ScanNet | | DIODE | | ETH3D | |
|---|---|---|---|---|---|---|---|---|---|---|---|
| | | AbsRel↓ | $\delta_1$↑ | AbsRel↓ | $\delta_1$↑ | AbsRel↓ | $\delta_1$↑ | AbsRel↓ | $\delta_1$↑ | AbsRel↓ | $\delta_1$↑ |
| MiDaS (Ranftl et al., 2020) | 2M | 0.236 | 0.630 | 0.111 | 0.885 | 0.121 | 0.846 | 0.332 | 0.715 | 0.184 | 0.752 |
| Omnidata (Eftekhar et al., 2021) | 12.2M | 0.149 | 0.835 | 0.074 | 0.945 | 0.075 | 0.936 | 0.339 | 0.742 | 0.166 | 0.778 |
| DPT-large (Ranftl et al., 2021) | 1.4M | 0.100 | 0.901 | 0.098 | 0.903 | 0.082 | 0.934 | 0.182 | 0.758 | 0.078 | 0.946 |
| DepthAnything (Yang et al., 2024a) | 63.5M | 0.080 | 0.946 | 0.043 | 0.980 | 0.043 | 0.981 | 0.261 | 0.759 | 0.058 | 0.984 |
| DepthAnything v2 (Yang et al., 2024b) | 62.6M | 0.080 | 0.943 | 0.043 | 0.979 | 0.042 | 0.979 | 0.321 | 0.758 | 0.066 | 0.983 |
| Metric3D v2 (Hu et al., 2024) | 16M | **0.052** | **0.979** | **0.039** | **0.979** | **0.023** | **0.989** | **0.147** | **0.892** | **0.040** | **0.983** |
| DiverseDepth (Yin et al., 2020) | 320K | 0.190 | 0.704 | 0.117 | 0.875 | 0.109 | 0.882 | 0.376 | 0.631 | 0.228 | 0.694 |
| LeReS (Yin et al., 2021) | 354K | 0.149 | 0.784 | 0.090 | 0.916 | 0.091 | 0.917 | 0.271 | 0.766 | 0.171 | 0.777 |
| HDN (Zhang et al., 2022) | 300K | 0.115 | 0.867 | 0.069 | 0.948 | 0.080 | 0.939 | 0.246 | **0.780** | 0.121 | 0.833 |
| Marigold (Ke et al., 2024) | 74K | 0.099 | 0.916 | 0.055 | 0.964 | 0.064 | 0.951 | 0.308 | 0.773 | **0.065** | 0.960 |
| GeoWizard (Fu et al., 2024b) | 280K | 0.129 | 0.851 | 0.059 | 0.959 | 0.066 | 0.953 | 0.328 | 0.753 | 0.077 | 0.940 |
| DepthFM (Gui et al., 2024) | 63K | 0.174 | 0.718 | 0.082 | 0.932 | 0.095 | 0.903 | 0.334 | 0.729 | 0.101 | 0.902 |
| DMP Official (Lee et al., 2024) | - | 0.240 | 0.622 | 0.109 | 0.891 | 0.146 | 0.814 | 0.361 | 0.706 | 0.128 | 0.857 |
| Our GenPercept (Depth) | 90K | 0.094 | 0.923 | **0.052** | 0.966 | **0.056** | **0.965** | 0.302 | 0.767 | 0.066 | 0.957 |
| Our GenPercept (Disparity) | 90K | 0.080 | 0.934 | 0.058 | **0.969** | 0.063 | 0.960 | **0.226** | 0.741 | 0.096 | 0.959 |
| Our GenPercept (Disparity + DPT head) | 90K | **0.078** | **0.935** | 0.059 | 0.967 | 0.064 | 0.961 | 0.228 | 0.740 | 0.094 | **0.961** |

Table 7: Quantitative comparison of surface normal estimation on three zero-shot datasets. We evaluate mean error↓, median error ↓ (med.), and the percentages of pixels ↑ with five thresholds.

| Method | Training Samples | NYU v2 | | | | | | | ScanNet | | | | | | | Sintel | | | | | | |
|---|---|---|---|---|---|---|---|---|---|---|---|---|---|---|---|---|---|---|---|---|---|---|
| | | mean | med. | 5.0° | 7.5° | 11.25° | 22.5° | 30° | mean | med. | 5.0° | 7.5° | 11.25° | 22.5° | 30° | mean | med. | 5.0° | 7.5° | 11.25° | 22.5° | 30° |
| Omnidata v1 (Eftekhar et al., 2021) | 12.2M | 23.1 | 12.9 | 21.6 | 33.4 | 45.8 | 66.3 | 73.6 | 22.9 | 12.3 | 21.5 | 34.5 | 47.4 | 66.1 | 73.2 | 41.5 | 35.7 | 3.0 | 5.8 | 11.4 | 30.4 | 42.0 |
| Ominidata v2 (Kar et al., 2022) | 12.2M | 17.2 | 9.7 | 25.3 | 40.2 | 55.5 | 76.5 | 83.0 | 16.2 | 8.5 | 29.1 | 44.9 | 60.2 | 79.5 | 84.7 | 40.5 | 35.1 | 4.6 | 7.9 | 14.7 | 33.0 | 43.5 |
| Metric3D v2 (Hu et al., 2024) | 8.8M | **13.5** | **6.7** | **40.1** | **53.5** | **65.9** | **82.6** | **87.7** | **11.8** | **5.5** | **46.6** | **60.7** | **71.6** | **85.4** | **89.7** | **22.8** | **14.2** | **18.4** | **28.5** | **41.6** | **66.7** | **75.8** |
| DINSE (Bae & Davison, 2024) | 160K | **16.4** | 8.4 | 32.8 | 46.3 | 59.6 | 77.7 | 83.5 | 16.2 | 8.3 | 29.8 | 45.9 | 61.0 | 78.7 | 84.4 | 34.9 | 28.1 | **8.9** | **14.1** | **21.5** | 41.5 | 52.7 |
| Geowizard (Fu et al., 2024b) | 280K | 19.8 | 11.2 | 18.0 | 32.7 | 50.2 | 73.0 | 79.9 | 21.1 | 11.9 | 15.9 | 29.7 | 47.4 | 70.7 | 77.8 | 36.1 | 28.4 | 4.1 | 8.6 | 16.9 | 39.8 | 52.5 |
| Our GenPercept (Latent MSE loss) | 90K | 17.4 | 9.5 | 23.3 | 40.0 | 56.3 | 76.8 | 83.0 | 16.3 | 8.9 | 25.8 | 42.7 | 59.6 | 79.4 | 84.8 | 44.4 | 31.6 | 3.4 | 7.5 | 15.0 | 37.0 | 48.0 |
| Our GenPercept (Image angular loss) | 90K | **16.4** | **8.0** | **33.3** | **47.8** | **60.9** | **78.3** | **83.7** | **15.2** | **7.4** | **33.9** | **50.7** | **65.0** | **80.9** | **85.7** | **34.6** | **26.2** | 5.2 | 9.8 | 18.4 | **43.8** | **55.8** |

compute the absolute relative error (AbsRel↓) and percentage of accurate valid depth pixels ($\delta_1$↑). Invalid regions are filtered out and the metrics are averaged on all images.

**Surface Normal Estimation.** The surface normal estimation aims to predict a vector perpendicular to tangent plane of the surface at each point P, which represents the orientation of the object's surface. For evaluation, we compute the angular error on three zero-shot datasets including NYU (Silberman et al., 2012), ScanNet (Dai et al., 2017), and Sintel (Butler et al., 2012). The mean ↓, median ↓, and the percentages of pixels ↑ with error below thresholds [5°, 7.5°, 11.25°, 22.5°, 30°] are reported. Invalid regions are filtered out and the metrics are averaged on all images.

**Quantitative Evaluation.** Quantitative results on monocular depth estimation and surface normal estimation are shown in table 6 and table 7, respectively. Even trained on limited synthetic datasets only, our GenPercept shows much robustness and achieves promising performance on diverse unseen scenes. For monocular depth models, we train them with pixel-wise MSE loss, scale-shift-invariant loss (Ranftl et al., 2020), and gradient loss (Ranftl et al., 2020). Furthermore, our disparity model (inverse of the depth) shows much better performance on datasets with outdoor scenes, such as KITTI and DIODE, but less performance on indoor datasets. Therefore, we suggest adopting the depth model for indoor scenes and the disparity model for outdoor scenes experimentally. By replacing the VAE decoder with a lightweight DPT head (Ranftl et al., 2021), GenPercept can infer faster without bearing the performance penalty. For surface normal estimation, the image angular loss brings significant performance improvement thanks to our one-step estimation paradigm.

**Qualitative Results.** Qualitative visualizations are shown in fig. 3. We observe excellent generalization of our models in that they can estimate accurate geometric information and promising details not only on diverse real and synthetic scenes, but also on comics, color drafts, and even sketches.

### 4.2 Image Segmentation

**Dichotomous Image Segmentation**. This is a category-agnostic, high-quality object segmentation task that accurately separates the object from the background in an image. Consistent with previous

Table 8: Quantitative results of dichotomous image segmentation on DIS5K validation and testing sets. Additional cross-dataset evaluation is provided in the supplementary material.

| Dataset | DIS-VD | | | | | | DIS-TE4 | | | | | | Overall DIS-TE (1-4) | | | | | |
|---|---|---|---|---|---|---|---|---|---|---|---|---|---|---|---|---|---|---|
| Metric | $maxF_\beta$ ↑ | $F_\beta^w$ ↑ | $M$ ↓ | $S_\alpha$ ↑ | $E_\phi^m$ ↑ | HCE$_\gamma$ ↓ | $maxF_\beta$ ↑ | $F_\beta^w$ ↑ | $M$ ↓ | $S_\alpha$ ↑ | $E_\phi^m$ ↑ | HCE$_\gamma$ ↓ | $maxF_\beta$ ↑ | $F_\beta^w$ ↑ | $M$ ↓ | $S_\alpha$ ↑ | $E_\phi^m$ ↑ | HCE$_\gamma$ ↓ |
| $U^2$Net (Qin et al., 2020) | 0.748 | 0.656 | 0.090 | 0.781 | 0.823 | 1413 | 0.795 | 0.705 | 0.087 | 0.807 | 0.847 | 3653 | 0.761 | 0.670 | 0.083 | 0.791 | 0.835 | 1333 |
| SINetV2 (Fan et al., 2021a) | 0.665 | 0.584 | 0.110 | 0.727 | 0.798 | 1568 | 0.699 | 0.616 | 0.113 | 0.744 | 0.824 | 3683 | 0.693 | 0.608 | 0.101 | 0.747 | 0.822 | 1411 |
| HySM (Nirkin et al., 2021) | 0.734 | 0.640 | 0.096 | 0.773 | 0.814 | 1324 | 0.782 | 0.693 | 0.091 | 0.802 | 0.842 | 3331 | 0.757 | 0.665 | 0.084 | 0.792 | 0.834 | 1218 |
| IS-Net (Qin et al., 2022) | 0.791 | 0.717 | 0.074 | 0.813 | 0.856 | 1116 | 0.827 | 0.753 | 0.072 | 0.830 | 0.870 | 2888 | 0.799 | 0.726 | 0.070 | 0.819 | 0.858 | 1016 |
| MVANet (Yu et al., 2024) | 0.904 | 0.861 | 0.035 | 0.909 | 0.937 | 878 | 0.911 | 0.857 | 0.041 | 0.903 | 0.944 | 2301 | 0.916 | 0.855 | 0.035 | 0.905 | 0.938 | 790 |
| Our Genpercept | 0.857 | 0.835 | 0.04 | 0.87 | 0.934 | 1511 | 0.848 | 0.829 | 0.049 | 0.854 | 0.938 | 3799 | 0.863 | 0.839 | 0.039 | 0.872 | 0.936 | 1364 |
| Our Genpercept (infer. at 1024px) | 0.877 | 0.859 | 0.035 | 0.887 | 0.941 | 1262 | 0.874 | 0.858 | 0.041 | 0.874 | 0.947 | 3321 | 0.875 | 0.856 | 0.036 | 0.885 | 0.939 | 1176 |

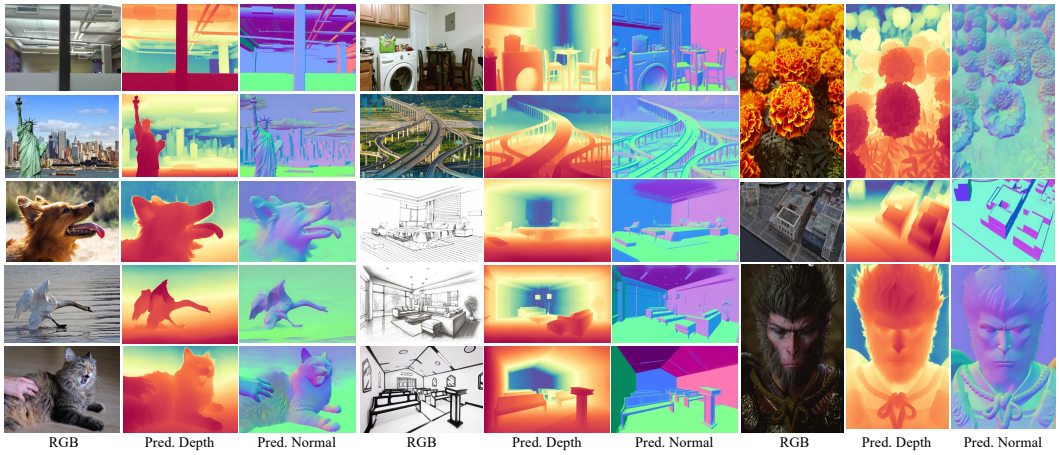


Figure 3: Qualitative results of monocular depth and surface normal estimation. The model works surprisingly well on *out-of-domain images (sketch and cartoon images).*

methods, we use the six evaluation metrics specified in the DIS task, which include maximal F-measure ($maxF_\beta$ ↑) (Achanta et al., 2009), weighted F-measure ($F_\beta^w$ ↑) (Margolin et al., 2014), mean absolute error ($M$ ↓) (Perazzi et al., 2012), structural measure ($S_\alpha$ ↑) (Fan et al., 2017), mean enhanced alignment measure ($E_\phi^m$ ↑) (Fan et al., 2018; 2021b) and human correction efforts ($\text{HCE}_\gamma$ ↓) (Qin et al., 2022). We choose DIS5K (Qin et al., 2022) as the training and testing dataset. We utilize DIS-TR for training and evaluate our model on DIS-VD and DIS-TE subsets. The pixel-wise MSE loss is utilized during training.

Quantitative results of dichotomous image segmentation are shown in table 8, respectively. We only show partial results due to paper page limitations, full comparisons are accessible in the supplementary material. GenPercept outperforms methods like HySM (Nirkin et al., 2021) and IS-Net (Qin et al., 2022) on this challenging dataset across most evaluation metrics, but there exists room for further improvement compared to SoTA methods like MVANet (Yu et al., 2024). As shown in Fig. 5, our approach provides a detailed foreground mask. For thin lines and meticulous objects that are difficult for previous methods to process, our method can also output accurate segmentation results.

**Semantic Image Segmentation.** This is a fundamental computer vision task that involves classifying each pixel in an image into a specific category or class. For training, we utilized the indoor synthetic dataset, HyperSim (Roberts et al., 2021), which comprises 40 semantic segmentation class labels. We encode different classes into 3-channel colormaps, treat the task as a regression problem, and fine-tune the original Stable Diffusion with the pixel-wise MSE loss. As demonstrated in fig. 4, the model generalizes well to classes within the HyperSim annotations, such as chairs and desks, but struggles with unrecognized categories such as cats and cars.

Another choice involves using a customized segmentation head. We incorporate a custom segmentation head, namely UperNet (Xiao et al., 2018), onto the multi-level features extracted by UNet. For the UperNet segmentation head, we follow the traditional semantic segmentation format to use n-channel output, where n is the number of categories. The quantitative results are presented in table 9, we test the model's performance on Hypersim (Roberts et al., 2021) and zero-shot ability on a subset of the ADE20k (Zhou et al., 2017) validation set, which contains overlapping classes. Besides, we compare with Mask2Former (Cheng et al., 2022) by training on ADE20K. GenPercept outperforms ResNet50 (He et al., 2016) and Swin-T (Liu et al., 2021) of Mask2Former but achieves lower performance than Swin-L (Liu et al., 2021).

Table 9: Quantitative results of semantic segmentation on Hypersim and ADE20k.

| Method | Training Dataset | mIoU↑ (Hypersim) | mIoU↑ (ADE20K) |
|---|---|---|---|
| GenPercept (Train UperNet) | Hypersim | 46.0 | 34.1 |
| GenPercept (Train U-Net + UperNet) | | 52.9 | 38.3 |
| Mask2Former R50 | ADE20K | - | 47.2 |
| Mask2Former Swin-T | | - | 47.7 |
| Mask2Former Swin-L | | - | 56.4 |
| GenPercept (Train U-Net + UperNet) | | - | 50.2 |

Table 10: Quantitative comparisons of image matting on the P3M-500-NP and AIM500.

| Method | Test Dataset | SAD ↓ | MAD ↓ | MSE ↓ | CONN ↓ |
|---|---|---|---|---|---|
| HATT (Qiao et al., 2020) | P3M-500-NP | 30.35 | 0.0176 | 0.0072 | 27.42 |
| SHM (Chen et al., 2018) | | 20.77 | 0.0122 | 0.0093 | 17.09 |
| MODNet (Ke et al., 2022) | | 16.70 | 0.0097 | 0.0051 | 13.81 |
| P3M-Net (Li et al., 2021) | | 11.23 | 0.0065 | 0.0035 | 12.51 |
| ViTAE-S (Ma et al., 2023) | | **7.59** | **0.0044** | **0.0019** | **6.96** |
| Our GenPercept | | 12.77 | 0.0074 | 0.0027 | 10.46 |
| ViTAE-S (Ma et al., 2023) | AIM500 (Zero-shot) | 112.52 | 0.0608 | 0.0602 | 43.18 |
| Our GenPercept | | **75.5** | **0.0444** | **0.0242** | **36.74** |

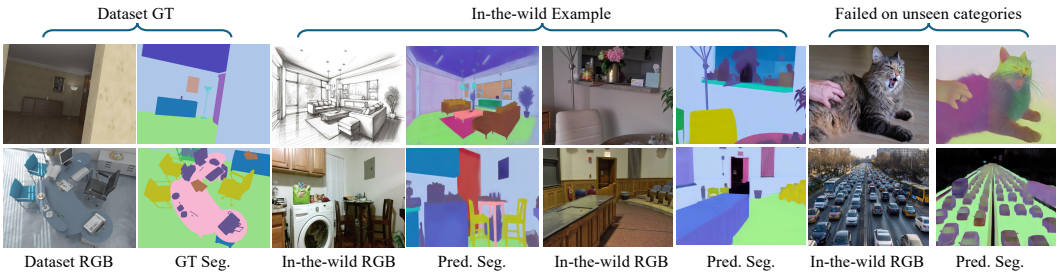


Figure 4: Quanlitative results of semantic segmentation in the wild. Trained on the synthetic indoor Hypersim dataset, GenPercept shows much robustness on the trained categories of complex in-the-wild images, *e.g.*, yellow chairs, green floor, and light blue wall. Due to the limited annotation categories and little negative label of "unknown category", it sometimes fails in outdoor scenes and unseen categories such as cats and cars.

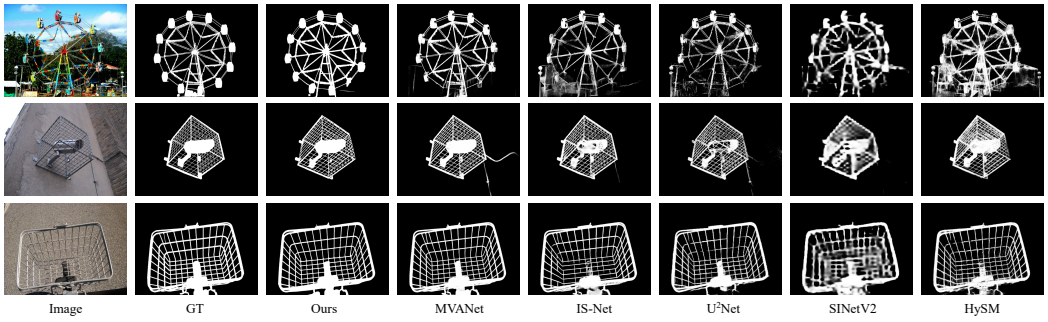


Figure 5: Qualitative comparison of dichotomous image segmentation.

### 4.3 Image Matting

**Task Definition.** Image matting aims to extract the foreground, background, and alpha mask from an image. Traditional approaches depend on supplementary inputs that delineate foreground, background, and ambiguous areas to reduce uncertainty. Automatic image matting seeks to remove this dependency by directly estimating these components from the image alone. The implementation details can be found in the supplementary material.

**Quantitative and Qualitative Results.** We evaluate metrics including the sum of absolute differences (SAD), mean squared error (MSE), mean absolute difference (MAD), gradient (Grad.), and Connectivity (Conn.) on the P3M-500-NP test set. SAD and MAD measure the mean L1 distance between predictions and ground truth labels. MSE and CONN focus on L2 distance and connectivity that better reflects human intuition. As shown in table 10, our GenPercept is less accurate compared with the state-of-the-art methods. However, when transferring the human image matting ability to general image matting tasks, GenPercept achieves much better performance. It proves the robustness brought by the prior knowledge of diffusion models pre-trained on the LAION dataset. Quantitative results of image matting are shown in fig. 6. Please see supplementary for more visualization results.

## 5 Related Work

**Vision Pre-Training.** Models pretrained on large-scale datasets possess powerful feature extraction capabilities, enabling them to be effectively transferred to a wide range of visual tasks. For instance, the ResNet (He et al., 2016) model pretrained on ImageNet (Russakovsky et al., 2015) can be fine-tuned and applied to perception tasks. By means of contrastive learning, MoCo (He et al., 2020) and CLIP (Radford et al., 2021) acquire rich visual and semantic representations, leveraging their advantages in joint visual and semantic modeling to enhance the performance of multimodal tasks. DINO (Caron et al., 2021), through self-distillation, endows Vision Transformer and convolutional networks with comparable visual representation quality and demonstrates that self-supervised ViT representations contain explicit semantic segmentation information. DINOv2 (Oquab et al., 2024)

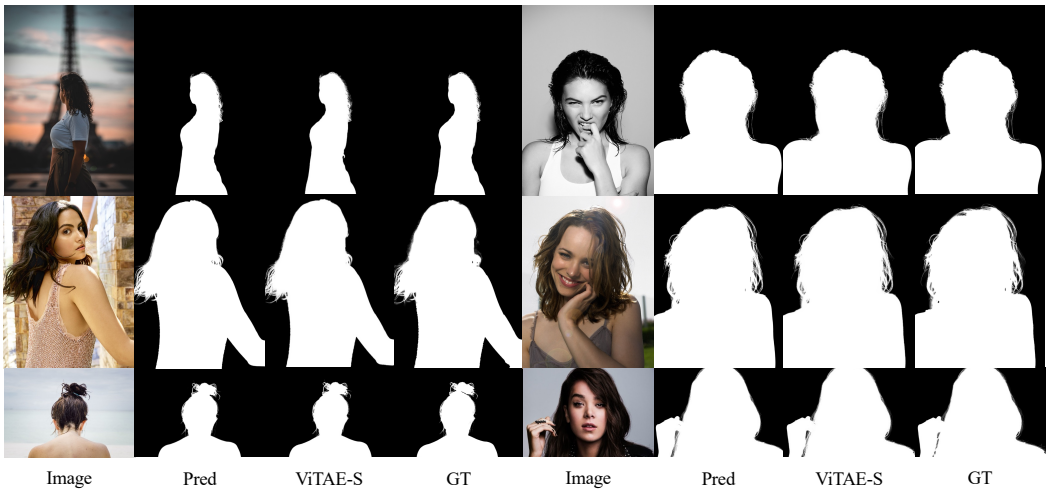


Figure 6: Visualization of image matting on the P3M-500-NP test set.

leverages self-supervised learning on a large curated dataset and exhibits remarkable zero-shot generalization capabilities across computer vision tasks at both image and pixel levels, including classification, semantic segmentation, and depth estimation. In our work, we leverage Stable Diffusion (Rombach et al., 2022) as a prior for scene understanding and transfer it to various perception tasks.

**Diffusion Priors for Dense Prediction.** Several works explore to use the priors of generative models for perceptual tasks. Some works (Bhattad et al., 2024; Du et al., 2023) demonstrate that generative models encode property maps of the scene. By finding latent variable offsets, using LoRA (Hu et al., 2022), etc., generative models can directly produce intrinsic images like surface normals, depth, albedo, etc. LDMSeg (Van Gansbeke & De Brabandere, 2024) devises an image-conditioned sampling process, enabling diffusion models to directly output panoptic segmentation. UniGS (Qi et al., 2023) proposes location-aware color encoding and decoding strategies, allowing diffusion models to support referring segmentation and entity segmentation. Marigold (Ke et al., 2024) fine-tunes diffusion model on limited synthetic data, enabling it to support affine-invariant monocular depth estimation and exhibit strong generalization performance. However, Marigold is time-consuming due to the need for multiple iterations of denoising. Additionally, the Gaussian noise leads to inconsistent results across inferences, requiring aggregation over multiple inferences. Xiang et al. (2023) train a denoising auto-encoder for image classification. The difference of their method compared with traditional denoising auto-encoder is that input images are encoded into a latent code and denoising is performed in the latent space rather than the pixel space. They show good results on very small-scale datasets (CIFAR and ImageNet-tiny) to prove the concept and no results were reported on larger datasets. Furthermore, GeoWizard (Fu et al., 2024a) extends the generative capabilities of Marigold, achieving better performance in joint depth and normal estimation, which enhances applications like 3D reconstruction and novel view synthesis. Moreover, DepthFM (Gui et al., 2024) addresses the speed challenge of Marigold by employing flow matching, offering a fast and efficient monocular depth estimation model.

## 6 Conclusion

In this work, we introduce GenPercept, an embarrassingly straightforward yet powerful approach to re-use the off-the-shelf UNet trained using diffusion processes. GenPercept demonstrates the capability to effectively leverage pre-trained diffusion models across a range of downstream dense perception tasks. We contend that our proposed methodology provides an efficient and potent paradigm for harnessing the capabilities of pre-trained diffusion models in dense visual perception tasks. For future research, we recommend investigating the impact of scaling up the volume of fine-tuning data and exploring the key components of pre-training by applying alternative self-supervised pre-training methods on the LAION dataset, such as Masked Autoencoders (MAE) or Contrastive Language-Image Pretraining (CLIP). It will be helpful to clarify whether the highly detailed visual predictions produced by existing diffusion models are primarily driven by the extensive LAION dataset or the diffusion pretraining paradigm itself.

## REFERENCES


Radhakrishna Achanta, Sheila Hemami, Francisco Estrada, and Sabine Susstrunk. Frequency-tuned salient region detection. In *Proc. IEEE Conf. Comp. Vis. Patt. Recogn.*, 2009.

Gwangbin Bae and Andrew J Davison. Rethinking inductive biases for surface normal estimation. In *Proc. IEEE Conf. Comp. Vis. Patt. Recogn.*, 2024.

Anand Bhattad, Daniel McKee, Derek Hoiem, and David Forsyth. Stylegan knows normal, depth, albedo, and more. *Proc. Advances in Neural Inf. Process. Syst.*, 2024.

D. J. Butler, J. Wulff, G. B. Stanley, and M. J. Black. A naturalistic open source movie for optical flow evaluation. In A. Fitzgibbon et al. (Eds.) (ed.), *Proc. Eur. Conf. Comp. Vis.*, Part IV, LNCS 7577, pp. 611–625. Springer-Verlag, October 2012.

Mathilde Caron, Hugo Touvron, Ishan Misra, Hervé Jégou, Julien Mairal, Piotr Bojanowski, and Armand Joulin. Emerging properties in self-supervised vision transformers. In *Proc. IEEE Int. Conf. Comp. Vis.*, pp. 9650–9660, 2021.

Junsong Chen, YU Jincheng, GE Chongjian, Lewei Yao, Enze Xie, Zhongdao Wang, James Kwok, Ping Luo, Huchuan Lu, and Zhenguo Li. Pixart-$\alpha$: Fast training of diffusion transformer for photorealistic text-to-image synthesis. In *Proc. Int. Conf. Learn. Representations*, 2023.

Quan Chen, Tiezheng Ge, Yanyu Xu, Zhiqiang Zhang, Xinxin Yang, and Kun Gai. Semantic human matting. *arXiv: Comp. Res. Repository*, 2018.

Xi Chen, Sida Peng, Dongchen Yang, Yuan Liu, Bowen Pan, Chengfei Lv, and Xiaowei Zhou. Intrinsicanything: Learning diffusion priors for inverse rendering under unknown illumination. *arXiv: Comp. Res. Repository*, 2024.

Bowen Cheng, Ishan Misra, Alexander G Schwing, Alexander Kirillov, and Rohit Girdhar. Masked-attention mask transformer for universal image segmentation. In *Proc. IEEE Conf. Comp. Vis. Patt. Recogn.*, pp. 1290–1299, 2022.

Marius Cordts, Mohamed Omran, Sebastian Ramos, Timo Rehfeld, Markus Enzweiler, Rodrigo Benenson, Uwe Franke, Stefan Roth, and Bernt Schiele. The cityscapes dataset for semantic urban scene understanding. In *Proc. IEEE Conf. Comp. Vis. Patt. Recogn.*, pp. 3213–3223, 2016.

Angela Dai, Angel X Chang, Manolis Savva, Maciej Halber, Thomas Funkhouser, and Matthias Nießner. Scannet: Richly-annotated 3d reconstructions of indoor scenes. In *Proc. IEEE Conf. Comp. Vis. Patt. Recogn.*, 2017.

Xiaodan Du, Nicholas Kolkin, Greg Shakhnarovich, and Anand Bhattad. Generative models: What do they know? do they know things? let's find out! *arXiv: Comp. Res. Repository*, 2023.

Ainaz Eftekhar, Alexander Sax, Jitendra Malik, and Amir Zamir. Omnidata: A scalable pipeline for making multi-task mid-level vision datasets from 3d scans. In *Proc. IEEE Int. Conf. Comp. Vis.*, 2021.

D Fan, M Cheng, Y Liu, T Li, and A Borji. A new way to evaluate foreground maps. In *Proc. IEEE Conf. Comp. Vis. Patt. Recogn.*, 2017.

Deng-Ping Fan, Cheng Gong, Yang Cao, Bo Ren, Ming-Ming Cheng, and Ali Borji. Enhanced-alignment measure for binary foreground map evaluation. In *Proc. International Joint Conf. Artificial Intelligence*, 2018.

Deng-Ping Fan, Ge-Peng Ji, Ming-Ming Cheng, and Ling Shao. Concealed object detection. *IEEE Trans. Pattern Anal. Mach. Intell.*, 2021a.

Deng-Ping Fan, Ge-Peng Ji, Xuebin Qin, and Ming-Ming Cheng. Cognitive vision inspired object segmentation metric and loss function. *Scientia Sinica Informationis*, 2021b.

Xiao Fu, Wei Yin, Mu Hu, Kaixuan Wang, Yuexin Ma, Ping Tan, Shaojie Shen, Dahua Lin, and Xiaoxiao Long. Geowizard: Unleashing the diffusion priors for 3d geometry estimation from a single image. In *Proc. Eur. Conf. Comp. Vis.*, 2024a.

Xiao Fu, Wei Yin, Mu Hu, Kaixuan Wang, Yuexin Ma, Ping Tan, Shaojie Shen, Dahua Lin, and Xiaoxiao Long. Geowizard: Unleashing the diffusion priors for 3d geometry estimation from a single image. In *Proc. Eur. Conf. Comp. Vis.*, 2024b.

Andreas Geiger, Philip Lenz, Christoph Stiller, and Raquel Urtasun. Vision meets robotics: The kitti dataset. *Int. J. Robotics Research*, 2013.

Ming Gui, Johannes S Fischer, Ulrich Prestel, Pingchuan Ma, Dmytro Kotovenko, Olga Grebenkova, Stefan Andreas Baumann, Vincent Tao Hu, and Björn Ommer. Depthfm: Fast monocular depth estimation with flow matching. *arXiv: Comp. Res. Repository*, 2024.

Kaiming He, Xiangyu Zhang, Shaoqing Ren, and Jian Sun. Deep residual learning for image recognition. In *Proc. IEEE Conf. Comp. Vis. Patt. Recogn.*, 2016.

Kaiming He, Haoqi Fan, Yuxin Wu, Saining Xie, and Ross Girshick. Momentum contrast for unsupervised visual representation learning. In *Proc. IEEE Conf. Comp. Vis. Patt. Recogn.*, 2020.

Jonathan Ho, Ajay Jain, and Pieter Abbeel. Denoising diffusion probabilistic models. *Proc. Advances in Neural Inf. Process. Syst.*, 2020.

Edward J Hu, Yelong Shen, Phillip Wallis, Zeyuan Allen-Zhu, Yuanzhi Li, Shean Wang, Lu Wang, and Weizhu Chen. LoRA: Low-rank adaptation of large language models. In *Proc. Int. Conf. Learn. Representations*, 2022.

Mu Hu, Wei Yin, Chi Zhang, Zhipeng Cai, Xiaoxiao Long, Hao Chen, Kaixuan Wang, Gang Yu, Chunhua Shen, and Shaojie Shen. Metric3d v2: A versatile monocular geometric foundation model for zero-shot metric depth and surface normal estimation. *arXiv: Comp. Res. Repository*, 2024.

Oğuzhan Fatih Kar, Teresa Yeo, Andrei Atanov, and Amir Zamir. 3d common corruptions and data augmentation. In *Proc. IEEE Conf. Comp. Vis. Patt. Recogn.*, 2022.

Bingxin Ke, Anton Obukhov, Shengyu Huang, Nando Metzger, Rodrigo Caye Daudt, and Konrad Schindler. Repurposing diffusion-based image generators for monocular depth estimation. In *Proc. IEEE Conf. Comp. Vis. Patt. Recogn.*, 2024.

Zhanghan Ke, Jiayu Sun, Kaican Li, Qiong Yan, and Rynson W.H. Lau. Modnet: Real-time trimap-free portrait matting via objective decomposition. In *Proc. AAAI Conf. Artificial Intell.*, 2022.

Peter Kocsis, Vincent Sitzmann, and Matthias Nießner. Intrinsic image diffusion for indoor single-view material estimation. In *Proc. IEEE Conf. Comp. Vis. Patt. Recogn.*, pp. 5198–5208, 2024.

Hsin-Ying Lee, Hung-Yu Tseng, Hsin-Ying Lee, and Ming-Hsuan Yang. Exploiting diffusion prior for generalizable dense prediction. In *Proc. IEEE Conf. Comp. Vis. Patt. Recogn.*, 2024.

Jizhizi Li, Sihan Ma, Jing Zhang, and Dacheng Tao. Privacy-preserving portrait matting. In *Proc. ACM Int. Conf. Multimedia*, 2021.

Ze Liu, Yutong Lin, Yue Cao, Han Hu, Yixuan Wei, Zheng Zhang, Stephen Lin, and Baining Guo. Swin transformer: Hierarchical vision transformer using shifted windows. In *Proc. IEEE Int. Conf. Comp. Vis.*, pp. 10012–10022, 2021.

Sihan Ma, Jizhizi Li, Jing Zhang, He Zhang, and Dacheng Tao. Rethinking portrait matting with privacy preserving. *Int. J. Comput. Vision*, 131(8):2172–2197, 2023.

Ran Margolin, Lihi Zelnik-Manor, and Ayellet Tal. How to evaluate foreground maps? In *Proc. IEEE Conf. Comp. Vis. Patt. Recogn.*, 2014.

Yuval Nirkin, Lior Wolf, and Tal Hassner. Hyperseg: Patch-wise hypernetwork for real-time semantic segmentation. In *Proc. IEEE Conf. Comp. Vis. Patt. Recogn.*, 2021.

Maxime Oquab, Timothée Darcet, Théo Moutakanni, Huy Vo, and Marc Szafraniec *et al.* DINOv2: Learning robust visual features without supervision. *Trans. Mach. Learn. Research*, 2024.

Federico Perazzi, Philipp Krähenbühl, Yael Pritch, and Alexander Hornung. Saliency filters: Contrast based filtering for salient region detection. In *Proc. IEEE Conf. Comp. Vis. Patt. Recogn.*, 2012.

Lu Qi, Lehan Yang, Weidong Guo, Yu Xu, Bo Du, Varun Jampani, and Ming-Hsuan Yang. Unigs: Unified representation for image generation and segmentation. *arXiv: Comp. Res. Repository*, 2023.

Yu Qiao, Yuhao Liu, Xin Yang, Dongsheng Zhou, Mingliang Xu, Qiang Zhang, and Xiaopeng Wei. Attention-guided hierarchical structure aggregation for image matting. In *Proc. IEEE Conf. Comp. Vis. Patt. Recogn.*, June 2020.

Xuebin Qin, Zichen Zhang, Chenyang Huang, Masood Dehghan, Osmar R Zaiane, and Martin Jagersand. U2-net: Going deeper with nested u-structure for salient object detection. *Pattern Recogn.*, 2020.

Xuebin Qin, Hang Dai, Xiaobin Hu, Deng-Ping Fan, Ling Shao, and Luc Van Gool. Highly accurate dichotomous image segmentation. In *Proc. Eur. Conf. Comp. Vis.*, 2022.

Alec Radford, Jong Wook Kim, Chris Hallacy, Aditya Ramesh, Gabriel Goh, Sandhini Agarwal, Girish Sastry, Amanda Askell, Pamela Mishkin, Jack Clark, et al. Learning transferable visual models from natural language supervision. In *Proc. Int. Conf. Mach. Learn.*, 2021.

René Ranftl, Katrin Lasinger, David Hafner, Konrad Schindler, and Vladlen Koltun. Towards robust monocular depth estimation: Mixing datasets for zero-shot cross-dataset transfer. *IEEE Trans. Pattern Anal. Mach. Intell.*, 2020.

René Ranftl, Alexey Bochkovskiy, and Vladlen Koltun. Vision transformers for dense prediction. In *Proc. IEEE Int. Conf. Comp. Vis.*, 2021.

Mike Roberts, Jason Ramapuram, Anurag Ranjan, Atulit Kumar, Miguel Angel Bautista, Nathan Paczan, Russ Webb, and Joshua M. Susskind. Hypersim: A photorealistic synthetic dataset for holistic indoor scene understanding. In *Proc. IEEE Int. Conf. Comp. Vis.*, 2021.

Robin Rombach, Andreas Blattmann, Dominik Lorenz, Patrick Esser, and Bjorn Ommer. High-resolution image synthesis with latent diffusion models. In *Proc. IEEE Conf. Comp. Vis. Patt. Recogn.*, 2022.

Olga Russakovsky, Jia Deng, Hao Su, Jonathan Krause, Sanjeev Satheesh, Sean Ma, Zhiheng Huang, Andrej Karpathy, Aditya Khosla, Michael Bernstein, et al. Imagenet large scale visual recognition challenge. *Int. J. Comput. Vision*, 115, 2015.

Thomas Schops, Johannes L Schonberger, Silvano Galliani, Torsten Sattler, Konrad Schindler, Marc Pollefeys, and Andreas Geiger. A multi-view stereo benchmark with high-resolution images and multi-camera videos. In *Proc. IEEE Conf. Comp. Vis. Patt. Recogn.*, 2017.

Nathan Silberman, Derek Hoiem, Pushmeet Kohli, and Rob Fergus. Indoor segmentation and support inference from rgbd images. In *Proc. Eur. Conf. Comp. Vis.*, 2012.

Jiaming Song, Chenlin Meng, and Stefano Ermon. Denoising diffusion implicit models. In *Proc. Int. Conf. Learn. Representations*, 2020.

Wouter Van Gansbeke and Bert De Brabandere. A simple latent diffusion approach for panoptic segmentation and mask inpainting. *arXiv: Comp. Res. Repository*, 2024.

Igor Vasiljevic, Nick Kolkin, Shanyi Zhang, Ruotian Luo, Haochen Wang, Falcon Z. Dai, Andrea F. Daniele, Mohammadreza Mostajabi, Steven Basart, Matthew R. Walter, and Gregory Shakhnarovich. DIODE: A Dense Indoor and Outdoor DEpth Dataset. *arXiv: Comp. Res. Repository*, 2019.

Weilai Xiang, Hongyu Yang, Di Huang, and Yunhong Wang. Denoising diffusion autoencoders are unified self-supervised learners. In *Proc. IEEE Int. Conf. Comp. Vis.*, 2023.

Tete Xiao, Yingcheng Liu, Bolei Zhou, Yuning Jiang, and Jian Sun. Unified perceptual parsing for scene understanding. In *Proc. Eur. Conf. Comp. Vis.*, 2018.

Lihe Yang, Bingyi Kang, Zilong Huang, Xiaogang Xu, Jiashi Feng, and Hengshuang Zhao. Depth anything: Unleashing the power of large-scale unlabeled data. In *Proc. IEEE Conf. Comp. Vis. Patt. Recogn.*, pp. 10371–10381, 2024a.

Lihe Yang, Bingyi Kang, Zilong Huang, Zhen Zhao, Xiaogang Xu, Jiashi Feng, and Hengshuang Zhao. Depth anything v2. *arXiv: Comp. Res. Repository*, 2024b.

Chongjie Ye, Lingteng Qiu, Xiaodong Gu, Qi Zuo, Yushuang Wu, Zilong Dong, Liefeng Bo, Yuliang Xiu, and Xiaoguang Han. Stablenormal: Reducing diffusion variance for stable and sharp normal. *arXiv: Comp. Res. Repository*, 2024.

Wei Yin, Xinlong Wang, Chunhua Shen, Yifan Liu, Zhi Tian, Songcen Xu, Changming Sun, and Dou Renyin. Diversedepth: Affine-invariant depth prediction using diverse data. *arXiv: Comp. Res. Repository*, 2020.

Wei Yin, Jianming Zhang, Oliver Wang, Simon Niklaus, Long Mai, Simon Chen, and Chunhua Shen. Learning to recover 3d scene shape from a single image. In *Proc. IEEE Conf. Comp. Vis. Patt. Recogn.*, 2021.

Qian Yu, Xiaoqi Zhao, Youwei Pang, Lihe Zhang, and Huchuan Lu. Multi-view aggregation network for dichotomous image segmentation. In *Proc. IEEE Conf. Comp. Vis. Patt. Recogn.*, pp. 3921–3930, 2024.

Amir R Zamir, Alexander Sax, William Shen, Leonidas J Guibas, Jitendra Malik, and Silvio Savarese. Taskonomy: Disentangling task transfer learning. In *Proc. IEEE Conf. Comp. Vis. Patt. Recogn.*, pp. 3712–3722, 2018.

Zheng Zeng, Valentin Deschaintre, Iliyan Georgiev, Yannick Hold-Geoffroy, Yiwei Hu, Fujun Luan, Ling-Qi Yan, and Miloš Hašan. Rgb $\leftrightarrow$ x: Image decomposition and synthesis using material-and lighting-aware diffusion models. In *ACM SIGGRAPH 2024 Conference Papers*, pp. 1–11, 2024.

Chi Zhang, Wei Yin, Billzb Wang, Gang Yu, Bin Fu, and Chunhua Shen. Hierarchical normalization for robust monocular depth estimation. *Proc. Advances in Neural Inf. Process. Syst.*, 2022.

Bolei Zhou, Hang Zhao, Xavier Puig, Sanja Fidler, Adela Barriuso, and Antonio Torralba. Scene parsing through ade20k dataset. In *Proc. IEEE Conf. Comp. Vis. Patt. Recogn.*, 2017.